

619 Sinusoidal voltage protocols for rapid characterization
620 of ion channel kinetics:
621 Supplementary Material

622 Kylie A. Beattie^{1,2}, Adam P. Hill^{3,4}, Rémi Bardenet⁵, Yi Cui⁶,
623 Jamie I. Vandenberg^{3,4}, David J. Gavaghan¹, Teun P. de Boer⁷, Gary R. Mirams^{1,8}

623 March 12, 2017

624 **A Additional Methods**

625 This section contains further description of the methods that were used, with a particular focus on
626 details of the Bayesian Inference scheme in Section A2. These sections do not feature in the Online
627 Methods purely due to space constraints.

628 **A1 Protocol schematics**

629 Figures A1–A3 show plots of the voltage clamps that are used in the repeated activation step and
630 activation kinetics protocols (Pr0–Pr2). The voltages and times of the steps are given in the Online
631 Methods 4.2.

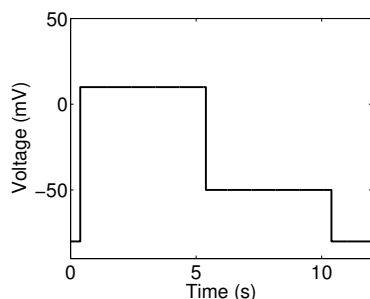


Figure A1: Repeated Activation Step Protocol (Pr0).

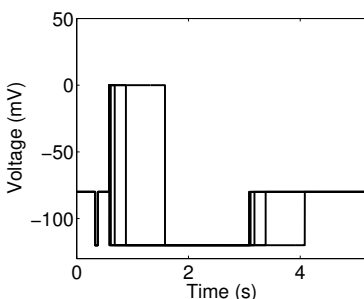


Figure A2: Activation Kinetics 1 Protocol (Pr1).

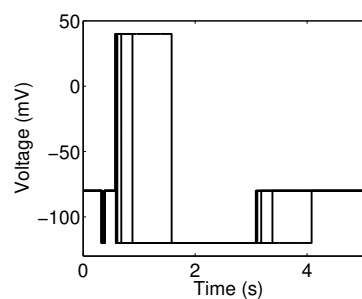


Figure A3: Activation Kinetics 2 Protocol (Pr2).

632 **A2 Bayesian Inference Scheme**

633 **A2.1 Conductance estimation to inform the prior**

634 Preliminary work revealed that using sine wave protocols alone often allowed kinetic parameters in
635 the hERG model to be recovered, but there was potential for identifiability problems (or at least
636 we encountered difficulties in finding a global optimum due to a rugged likelihood surface) when
637 simultaneously fitting the conductance parameter and transition rate parameters P_1 to P_8 (although

638 previous work suggests all parameters are theoretically identifiable⁴²). To add extra information
639 on conductance, we incorporated a voltage-step to +40 mV followed by a step down to -120 mV,
640 as described in the definition of the sine wave protocol in Section 4.2. The aim being to provoke
641 a large current. We then fitted a single exponential through the slow time constant of the tail
642 current exhibited during the -120 mV step (fitting was performed in the Clampfit software, using
643 the Levenberg-Marquardt algorithm with a tolerance of 10^{-6}). We then extrapolated back to the
644 point at which the voltage step to -120 mV was made, and used the extrapolated current value
645 at this point to estimate a conductance at this time point (this extrapolation method is described
646 in Vandenberg *et al.*²). The conductance we estimated was used as a lower bound for the prior
647 distribution of the conductance, as we describe below.

648 A2.2 Prior

649 In this section we describe our prior assumptions on the values that each model parameter can take.
650 The prior for the conductance G_{Kr} is assumed to be independent of the kinetic parameters, and to
651 take a uniform distribution. As discussed above, the lower bound is formed by estimating a lower
652 bound on the conductance value ‘directly’ from the experimental data; the upper bound is assumed
653 to be 10 times the value of the lower bound.

654 The other model parameters are within transition rates of the form

$$k = A \exp(BV), \tag{A.1}$$

655 where V is voltage and A and B are model parameters (P_1 to P_8 for k_1 to k_4 , as shown in Figure 3).

656 For parameters of the form A we assumed that the prior distribution is uniform between 10^{-7}
657 and 1000 ms^{-1} , again to cover (and extend beyond) the full physiological range expected with hERG
658 channel gating.

659 We assume that the prior distributions for B parameters are uniform between 10^{-7} and 0.4
660 mV^{-1} . The lower bound for this parameter was selected as the voltage-dependence becomes prac-
661 tically redundant when B becomes small: when $B = 10^{-7}$ the value of $\exp(BV)$ will change by less
662 than 0.0015% across the voltages we reach in this study. The upper value is beyond the physiolog-
663 ically expected range.

664 We also impose a prior on the maximum rate of transition k between any states (maximum
665 across the full voltage range in the protocol (that is from -120 to 58.25 mV)). If the maximum
666 rate k is greater than 1000 ms^{-1} , or less than $1.67 \times 10^{-5} \text{ ms}^{-1}$, the pair of parameter values that
667 give rise to this are assigned prior probability zero (strictly, this is equivalent to defining 2D prior
668 on A and B , but is easier to describe here, and code, as an additional constraint): the lower bound
669 is based on the assumption that a transition is not physiologically realistic if it occurs over a time
670 scale slower than one minute; the upper bound was decided based on the prior for the individual
671 parameters A and B in the transition rate expression and to prevent the transitions occurring over
672 a time scale much faster than would be physiologically expected.

673 Note that our analysis is relatively insensitive to the precise form of the prior that is used as
674 there are around 80,000 data points (8s of 10 kHz samples) in the likelihood product calculation
675 of Equation (13), which is then also in a product with the prior in Equation (12). So, effectively,
676 each of the 10,000 data points has the same impact as the prior does on the posterior. Given
677 our likelihood is extremely peaked around its maximum (Figure 3C), we have observed no notable
678 influence of the shape of the prior, as long as the maximum posterior density point is well away from
679 the limits described above — which it has been in all cases. Note that the same concept means
680 that, in our case, the “maximum likelihood estimate” (MLE — parameter set that maximizes

681 Equation (13)) would be practically indistinguishable from the “maximum a posteriori estimator”
682 (MAP — parameter set that maximizes Equation (12)) even if we had a non-uniform prior.

683 **A2.3 Global minimization**

684 The Covariance Matrix Adaptation — Evolution Strategy (CMA-ES) algorithm was used to perform
685 an initial exploration of the surface of the posterior density, and to identify parameter sets which
686 allow the model to fit the experimental data well. The tolerance used is 10^{-4} and all other settings
687 are the defaults in MatLab implementation of CMA-ES v3.61, downloaded from [https://www.lri.](https://www.lri.fr/~hansen/cmaes.m)
688 [fr/~hansen/cmaes.m](https://www.lri.fr/~hansen/cmaes.m). We imposed bounds based on the prior as we describe above in Section A2.2.

689 We run the CMA-ES algorithm from different starting points and continue to do so until we
690 identify the same region of parameter space for optimal parameter sets for each experimental data
691 trace when starting from many different starting points. In this way, we can be confident that we
692 identify the same region of high likelihood consistently (not simply the first local minimum that is
693 found), and we have more confidence that this corresponds to the globally optimal likelihood.

694 These initial starting points for the CMA-ES algorithm are sampled from within the prior
695 defined for each parameter, described in section A2.2. To sample from the prior we simply select
696 the voltage-dependent transition rate parameters (of the form B described above) uniformly from
697 the defined range. The same approach is used to sample the conductance parameter.

698 For the parameters of the form A above we sample starting points in a logarithmic fashion across
699 the range of the uniform prior. This approach helps to restrict the initial guesses of parameters to
700 the region of measurable time scales we imposed by defining the maximum and minimum ranges on
701 the overall transition rate, as described above. We also run a small selection of starting points with
702 both A and B parameter values sampled uniformly from $[10^{-7}, 0.1]$ (the range in which most existing
703 model parameters lie), again to ensure we identify the global optimal solution to the optimization
704 problem. We log-transform all parameters within CMA-ES to aid the optimization process by
705 making all values similar orders of magnitude.

706 **A2.4 Markov Chain Monte Carlo parameter inference**

707 We use *Markov Chain Monte Carlo* (MCMC) methods to explore the posterior probability distri-
708 bution. The approach we use is the *Metropolis-Hastings* algorithm. In this algorithm, candidate
709 parameter sets are proposed from a *proposal distribution* $q(\theta_{\text{cand}}|\theta_i)$ which depends only on the
710 previously accepted parameter set θ_i . We use a multivariate normal distribution as our proposal
711 distribution. Any candidate parameter set θ_{cand} is compared to the current parameter set θ_i by
712 calculating the ratio of the likelihood of the two parameter sets. The value of the ratio determines
713 whether or not the proposed parameter set is accepted as part of the MCMC chain. If the can-
714 didate parameter set has a greater posterior density value than the existing parameter set then
715 it will be added to the Markov chain, that is $\theta_{i+1} = \theta_{\text{cand}}$. Otherwise, the parameter set may
716 still be accepted with a probability equal to the ratio of likelihood/posterior density values. That
717 is, a proposed parameter set generated from a multivariate normal distribution is accepted with
718 probability

$$\alpha = \min \left\{ \frac{L(\theta_{\text{cand}}|\mathbf{y})}{L(\theta_i|\mathbf{y})}, 1 \right\}. \quad (\text{A.2})$$

719 Also note that if the proposed parameter set contains any parameters outside the range of the
720 prior, or violates any of the conditions on the parameters that we have imposed, the parameter set
721 is assigned an acceptance probability of 0 and immediately rejected and the previously accepted
722 parameter set is again added to the Markov chain — that is, $\theta_{i+1} = \theta_i$.

723 In practice, we use a covariance matrix adaptive version of the Metropolis-Hastings Algorithm
 724 which helps identify the directions in parameter space which have the highest likelihood values, the
 725 algorithm is described in Haario *et al.*⁴³. At each iteration of the algorithm, the covariance matrix
 726 of the multivariate normal distribution is updated and a scalar value is also updated to define the
 727 width of the distribution. We run our MCMC chains for 250,000 samples and discard the first
 728 50,000 samples as ‘burn in’ (for an introduction to MCMC see Gilks *et al.*⁴⁴).

729 B Details of Published hERG Channel Models

730 Figure 1A of the main text features simulations from 29 literature hERG or I_{Kr} models. In Table B1
 731 we list these models, give references, and show the seven different structures that they feature in
 732 Figure B4.

733 There are two models in this table that are not in Figure 1A: the Kiehn *et al.*⁴⁵ model as it
 734 is defined only at certain voltages; and the Piper *et al.*⁴⁶ model as it does not easily fit into the
 735 Hodgkin-Huxley/Markov model framework we used in our simulation code.

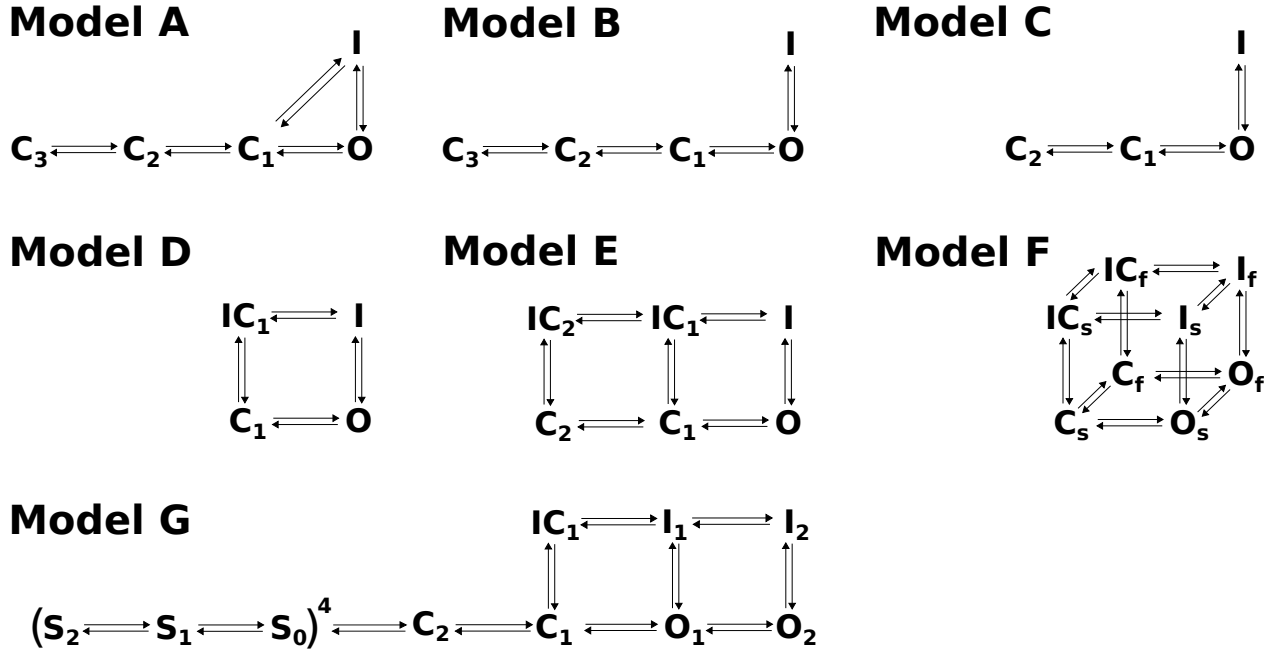


Figure B4: Different mathematical model structures for the literature models listed in Table B1. The model we use in the main text takes structure D as shown in Figure 3B.

Table B1: Table summarizing details of each published I_{Kr} model formulation, in chronological order. ‘# Params’ indicates the total number of free parameters (the number given includes a G_{Kr} parameter for the conductance). The *Model Type* is ‘HH’ for Hodgkin–Huxley models and ‘MM’ for Markov Models, or a hybrid of the two (MM/HH, which generally means a MM with some symmetry in transition rates).

Model	Model Type	# Params	Experimental Cell Type	Temperature	Structure in Figure B4
Zeng <i>et al.</i> ³⁰	HH	11	Guinea pig ventricular myocytes	Physiological	D
Lindblad <i>et al.</i> ⁴⁷	HH	11	Rabbit SA, AV, atrial myocytes and rabbit and guinea pig ventricular myocytes	Physiological	D
Liu <i>et al.</i> ⁴⁸	MM	11	Ferret atrial myocytes	Room	C
Wang <i>et al.</i> ²⁵	MM	15	<i>Xenopus</i> oocytes	Room	B
Courtemanche <i>et al.</i> ⁴⁹	HH	10	Human atrial myocytes	Physiological	D
Nygren <i>et al.</i> ⁵⁰	HH	9	Human atrial/rabbit atrial myocytes and <i>Xenopus</i> oocytes	Physiological	D
Priebe & Beuckelmann ⁵¹	HH	9	Human ventricular myocytes	Physiological	D
Kiehn <i>et al.</i> ⁴⁵	MM	9*	<i>Xenopus</i> oocytes	Room	A
Winslow <i>et al.</i> ⁵²	HH	7	Guinea pig ventricular myocytes	Physiological	D
Ramirez <i>et al.</i> ⁵³	HH	13	Canine atrial myocytes	Physiological	D
Zhang <i>et al.</i> ⁵⁴	HH	15	Rabbit sino-atrial node cells	Physiological	F
Clancy & Rudy ⁵⁵	MM	14	Guinea pig ventricular	Physiological	A
Lu <i>et al.</i> ⁵⁶	MM	17	Chinese Hamster Ovary (CHO)	Physiological	A
Mazhari <i>et al.</i> ³¹	MM	17	Human Embryonic Kidney (HEK) 293	Physiological	A
Fox <i>et al.</i> ⁵⁷	HH	10	Canine ventricular myocytes	Physiological	D
Kurata <i>et al.</i> ⁵⁸	HH	18	Rabbit sino-atrial node cells	Physiological	F
Oehmen <i>et al.</i> ⁵⁹	MM	11	Rabbit sino-atrial cells	Physiological	C
Matsuoka <i>et al.</i> ⁶⁰	HH	23	Rabbit pacemaker and guinea pig ventricular myocytes	Physiological	F
Piper <i>et al.</i> ⁴⁶	MM/HH	43	<i>Xenopus</i> oocytes	Room	G
Seemann <i>et al.</i> ⁶¹	HH	7	Human ventricular myocytes	Physiological	D
Hund & Rudy ⁶²	HH	11	Canine ventricular myocytes	Physiological	D
Shannon <i>et al.</i> ⁶³	HH	11	Rabbit ventricular myocytes	Physiological	D
Ten Tusscher <i>et al.</i> ³²	HH	13	HEK 293/CHO/ <i>Xenopus</i> oocytes	Physiological	D
Fink <i>et al.</i> ⁶⁴	MM	15	Human Embryonic Kidney (HEK) 293	Physiological	B
Aslanidi <i>et al.</i> ⁶⁵	HH	8	Canine Purkinje cells	Physiological	D
Inada <i>et al.</i> ⁶⁶	HH	20	Rabbit atrio-ventricular node cells	Physiological	F
Grandi <i>et al.</i> ⁶⁷	HH	12	Human ventricular myocytes	Physiological	D
O’Hara <i>et al.</i> ⁶⁸	HH	19	Human ventricular myocytes	Physiological	F
Severi <i>et al.</i> ⁶⁹	HH	17	Rabbit sino-atrial node cells	Physiological	F
Di Veroli <i>et al.</i> ³³	MM/HH	13	Chinese Hamster Ovary (CHO)	Room	E
Di Veroli <i>et al.</i> ³³	HH	17	Human Embryonic Kidney (HEK293) expressing canine ERG	Physiological	D

* The transition rates of the Kiehn *et al.*⁴⁵ model are defined at specific voltages, so for this model there are 8 parameters (and 1 conductance parameter) for each voltage at which the model is defined.

736 C Synthetic Data Study to Assess Protocol Information Content

737 In order to verify that there was sufficient information within the sinusoidal voltage protocol to
738 parameterize our model we performed a synthetic data study. The aim in such a study is to
739 ascertain whether we can recover the parameters used in the simulation from a simulated data trace
740 (with added noise in this case).

741 C1 Producing synthetic data

742 In order to produce synthetic data we simulated the mathematical model with the parameter values
743 obtained when fitting to the experimental data trace. We scale the simulated trace by multiplying
744 by this factor, so it becomes approximately the same magnitude (in nA) as the experimental trace.
745 We estimated the typical level of noise from the experimental trace by calculating the standard
746 deviation σ of the experimental current during the first 200 ms (where the current is around zero at
747 the initial holding potential of -80 mV). We then generate a synthetic data trace by adding normally
748 distributed noise with a mean of zero and the standard deviation equal to the noise estimated from
749 the experimental trace ($\sim N(0, \sigma^2)$) to the conductance-scaled simulated trace.

750 The example we present here uses the experimental reference trace from cell 5, featured in much
751 of the manuscript.

752 C2 Inferring parameters from synthetic data

753 We then attempt to infer parameters from this ‘synthetic data’ trace, using the CMA-ES algorithm
754 followed by MCMC as described in Section 4.7. In Figure C5 we present probability density distri-
755 butions obtained when using both synthetic and experimental traces. We are able to recover the
756 original parameters underlying the synthetic trace with high accuracy.

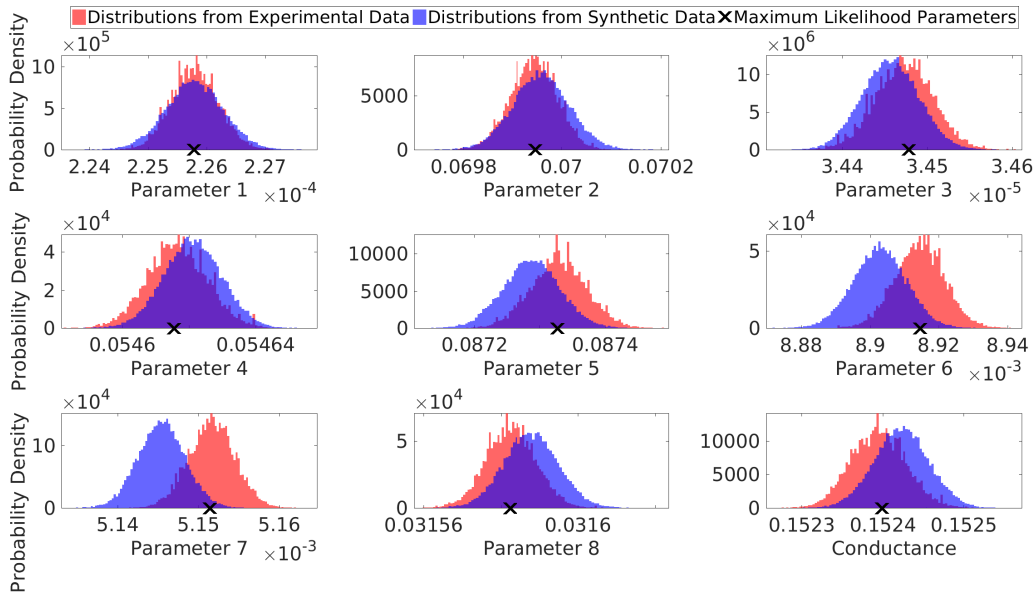


Figure C5: Probability density distributions for each parameter estimates from fitting to both experimental data (red) and simulated data (blue). Crosses indicate the parameter set with the maximum posterior density.

757 The synthetic data study provides us with confidence in the suitability of our protocol for
758 accurately identifying parameters of the model presented in Figure 3B in the main text, and also
759 that the parameter inference protocol(s) we are using are suitable for the task. We believe such an
760 approach should always be used to test whether there is sufficient information in the experimental
761 data being proposed for calibration of a mathematical model. The test should be performed twice:
762 before conducting the experiment (with the pre-existing best guess at the parameters); and also after
763 conducting the experiment (with the new maximum posterior density estimate of the parameters
764 — as we illustrate in Figure C5).



D Cell-Specific versus Literature Model Predictions

In Tables D2–D10 we compare the predictions given by each cell-specific model with a range of literature model predictions. We compare their ability to predict the full current traces for the validation protocols Pr3–6 discussed in the main text. Each table provides the mean (over each time point) square difference between an experimental current recording in one particular cell and its cell-specific model prediction under each of the validation protocols, and compares this with current predictions from a range of literature models. Equation (F.3) gives the formula that was used to calculate the error entries.



Note that we have to choose a conductance value, G_{K_r} , for the literature models. G_{K_r} is selected differently for each cell by minimizing the error metric for the predicted current trace under the action potential protocol (Pr6) for each model (a best-case scenario for each literature model). Our new cell-specific models’ conductances were fitted to the sine wave protocol (Pr7), along with the rest of their parameters. N.B. the literature model predictions are worse if we scale them to fit the sine wave; we considered this perhaps unjustified since they were developed never having seen such a protocol.

Despite literature models having their conductance scaled to minimize error in the Pr6 (action potential clamp) current prediction; only the Wang *et al.*²⁵ model for Cells #1, #3 and #4, and the Di Veroli *et al.*³³ model for Cell #9 perform better than our cell-specific models. The sine-wave fitted model outperforms all other literature models for all other cells.


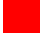
Additionally, the Wang *et al.*²⁵ model gives better predictions for the deactivation protocol current for some cells; and for the inactivation protocol for Cell #9. The Di Veroli *et al.*³³ model gives better predictions for the inactivation protocol for Cells #5 and #9; and the deactivation protocol for Cell #6.

Table D2: Table quantifying square root of mean square difference (units nA) between experimental current traces and simulation predictions for the validation protocols shown in Figures 4 and 5 for Cell #1. Here the color scale is set so that  represents zero error and  represents the highest error for each protocol/column.



Model	Sine Wave (Pr7)	AP (Pr6)	Steady Act. (Pr3)	Deact. (Pr4)	Inact. (Pr5)
New model for Cell #1	0.0268	0.0757	0.0745	0.2115	0.1312
Wang <i>et al.</i> ²⁵	0.1196	0.0746	0.2079	0.2574	0.1543
Di Veroli <i>et al.</i> ³³	0.1406	0.0910	0.2097	0.3005	0.1706
Mazhari <i>et al.</i> ³¹	0.1213	0.0885	0.1962	0.3171	0.1619
Ten Tusscher <i>et al.</i> ³²	0.1827	0.1079	0.2563	0.3335	0.2265
Zeng <i>et al.</i> ³⁰	0.1928	0.1381	0.2961	0.3617	0.2275

Table D3: Table quantifying square root of mean square difference (units nA) between experimental current traces and simulation predictions for the validation protocols shown in Figures 4 and 5 for Cell #2. Here the color scale is set so that  represents zero error and  represents the highest error for each protocol/column.



Model	Sine Wave (Pr7)	AP (Pr6)	Steady Act. (Pr3)	Deact. (Pr4)	Inact. (Pr5)
New model for Cell #2	0.0262	0.0549	0.0481	0.1421	0.0478
Wang <i>et al.</i> ²⁵	0.0923	0.0732	0.1081	0.1075	0.0818
Di Veroli <i>et al.</i> ³³	0.0687	0.0564	0.0859	0.1427	0.0655
Mazhari <i>et al.</i> ³¹	0.0618	0.0664	0.0882	0.1793	0.0629
Ten Tusscher <i>et al.</i> ³²	0.1280	0.1159	0.1460	0.1902	0.1518
Zeng <i>et al.</i> ³⁰	0.1356	0.1395	0.1835	0.2190	0.1497

Table D4: Table quantifying square root of mean square difference (units nA) between experimental current traces and simulation predictions for the validation protocols shown in Figures 4 and 5 for Cell #3. Here the color scale is set so that  represents zero error and  represents the highest error for each protocol/column.


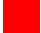
Model	Sine Wave (Pr7)	AP (Pr6)	Steady Act. (Pr3)	Deact. (Pr4)	Inact. (Pr5)
New model for Cell #3	0.0348	0.0997	0.0917	0.1320	0.1106
Wang <i>et al.</i> ²⁵	0.1015	0.0900	0.1071	0.1030	0.1178
Di Veroli <i>et al.</i> ³³	0.1365	0.1298	0.1639	0.1660	0.1502
Mazhari <i>et al.</i> ³¹	0.1167	0.1263	0.1404	0.1885	0.1599
Ten Tusscher <i>et al.</i> ³²	0.1833	0.1337	0.1603	0.1929	0.1953
Zeng <i>et al.</i> ³⁰	0.2024	0.1826	0.2123	0.2272	0.1971

Table D5: Table quantifying square root of mean square difference (units nA) between experimental current traces and simulation predictions for the validation protocols shown in Figures 4 and 5 for Cell #4. Here the color scale is set so that  represents zero error and  represents the highest error for each protocol/column.



Model	Sine Wave (Pr7)	AP (Pr6)	Steady Act. (Pr3)	Deact. (Pr4)	Inact. (Pr5)
New model for Cell #4	0.0346	0.0649	0.0931	0.1337	0.0864
Wang <i>et al.</i> ²⁵	0.0962	0.0624	0.0804	0.0736	0.0928
Di Veroli <i>et al.</i> ³³	0.0713	0.0871	0.1381	0.1462	0.1028
Mazhari <i>et al.</i> ³¹	0.0744	0.0992	0.1098	0.1828	0.1249
Ten Tusscher <i>et al.</i> ³²	0.1374	0.1350	0.1268	0.1771	0.1663
Zeng <i>et al.</i> ³⁰	0.1545	0.1867	0.1939	0.2194	0.1713

Table D6: Table quantifying square root of mean square difference (units nA) between experimental current traces and simulation predictions for the validation protocols shown in Figures 4 and 5 for Cell #5. Here the color scale is set so that  represents zero error and  represents the highest error for each protocol/column.



Model	Sine Wave (Pr7)	AP (Pr6)	Steady Act. (Pr3)	Deact. (Pr4)	Inact. (Pr5)
New model for Cell #5	0.0338	0.1003	0.0964	0.2788	0.5713
Wang <i>et al.</i> ²⁵	0.1409	0.1185	0.2236	0.2856	0.5715
Di Veroli <i>et al.</i> ³³	0.1498	0.1648	0.2086	0.3864	0.5659
Mazhari <i>et al.</i> ³¹	0.1400	0.1760	0.1982	0.4443	0.5726
Ten Tusscher <i>et al.</i> ³²	0.2643	0.2453	0.3169	0.4653	0.6482
Zeng <i>et al.</i> ³⁰	0.2845	0.3116	0.4001	0.5245	0.6262

Table D7: Table quantifying square root of mean square difference (units nA) between experimental current traces and simulation predictions for the validation protocols shown in Figures 4 and 5 for Cell #6. Here the color scale is set so that  represents zero error and  represents the highest error for each protocol/column.



Model	Sine Wave (Pr7)	AP (Pr6)	Steady Act. (Pr3)	Deact. (Pr4)	Inact. (Pr5)
New model for Cell #6	0.0149	0.0419	0.0482	0.0883	0.0443
Wang <i>et al.</i> ²⁵	0.0396	0.0503	0.0537	0.0412	0.0528
Di Veroli <i>et al.</i> ³³	0.0362	0.0569	0.0596	0.0794	0.0458
Mazhari <i>et al.</i> ³¹	0.0511	0.0621	0.0603	0.1048	0.0560
Ten Tusscher <i>et al.</i> ³²	0.0788	0.0844	0.0776	0.1041	0.1014
Zeng <i>et al.</i> ³⁰	0.0867	0.1101	0.1051	0.1255	0.0988

Table D8: Table quantifying square root of mean square difference (units nA) between experimental current traces and simulation predictions for the validation protocols shown in Figures 4 and 5 for Cell #7. Here the color scale is set so that  represents zero error and  represents the highest error for each protocol/column.

Model	Sine Wave (Pr7)	AP (Pr6)	Steady Act. (Pr3)	Deact. (Pr4)	Inact. (Pr5)
New model for Cell #7	0.0825	0.1343	0.2060	0.3167	0.1239
Wang <i>et al.</i> ²⁵	0.1914	0.2176	0.2506	0.2358	0.2726
Di Veroli <i>et al.</i> ³³	0.1994	0.2654	0.2827	0.4101	0.2605
Mazhari <i>et al.</i> ³¹	0.2361	0.2987	0.2597	0.5102	0.2637
Ten Tusscher <i>et al.</i> ³²	0.3966	0.4124	0.4205	0.5287	0.5326
Zeng <i>et al.</i> ³⁰	0.4147	0.5013	0.5597	0.6246	0.5357

Table D9: Table quantifying square root of mean square difference (units nA) between experimental current traces and simulation predictions for the validation protocols shown in Figures 4 and 5 for Cell #8. Here the color scale is set so that  represents zero error and  represents the highest error for each protocol/column.

Model	Sine Wave (Pr7)	AP (Pr6)	Steady Act. (Pr3)	Deact. (Pr4)	Inact. (Pr5)
New model for Cell #8	0.0426	0.1331	0.1302	0.1796	0.2222
Wang <i>et al.</i> ²⁵	0.1043	0.1367	0.2036	0.2100	0.2491
Di Veroli <i>et al.</i> ³³	0.1053	0.1545	0.1828	0.2656	0.2538
Mazhari <i>et al.</i> ³¹	0.1071	0.1621	0.1860	0.3058	0.2528
Ten Tusscher <i>et al.</i> ³²	0.1839	0.1957	0.2624	0.3248	0.3334
Zeng <i>et al.</i> ³⁰	0.1902	0.2305	0.3122	0.3641	0.3347

Table D10: Table quantifying square root of mean square difference (units nA) between experimental current traces and simulation predictions for the validation protocols shown in Figures 4 and 5 for Cell #9. Here the color scale is set so that  represents zero error and  represents the highest error for each protocol/column.

Model	Sine Wave (Pr7)	AP (Pr6)	Steady Act. (Pr3)	Deact. (Pr4)	Inact. (Pr5)
New model for Cell #9	0.0243	0.1478	0.1109	0.1806	0.2183
Wang <i>et al.</i> ²⁵	0.0507	0.1493	0.1277	0.1755	0.2181
Di Veroli <i>et al.</i> ³³	0.0474	0.1474	0.1153	0.1830	0.2164
Mazhari <i>et al.</i> ³¹	0.0408	0.1482	0.1176	0.1917	0.2163
Ten Tusscher <i>et al.</i> ³²	0.0773	0.1547	0.1443	0.1961	0.2246
Zeng <i>et al.</i> ³⁰	0.0820	0.1606	0.1589	0.2060	0.2253

788 **E Additional Peak Current-Voltage Relationship Predictions**

789 Here we show the remainder of the predictions of the current-voltage relationships for the validation
 790 data of cell 5 that were not included in the main text (the results of Pr1 and Pr2). Figure E6 shows
 791 the summary curves for Pr1 (voltage clamp shown in Figure A2) and Pr2 (voltage clamp shown in
 792 Figure A3).

793 Traditionally these peak current curves would be plotted by normalizing to the peak current
 794 recorded in each activation kinetics protocol. However, as we have used a shorter version of the
 795 activation kinetics protocol, we do not expect that the channel would be fully open at the longest
 796 duration test step in Pr1 and Pr2. We have therefore instead normalized the curves using the peak
 797 current during the initial deactivation step in the sine wave protocol (around 1.6 seconds) where we
 798 expect the channel to be maximally open.

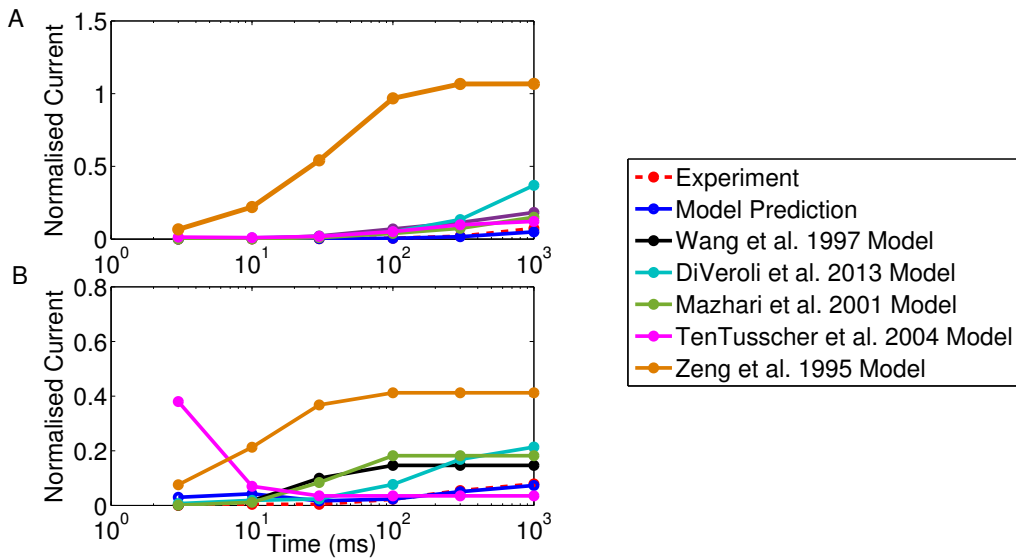


Figure E6: Predictions of peak current-voltage relationship derived from experiment and model predictions in response to; A) Activation Kinetics Pr1, B) Activation Kinetics Pr2, with comparison of our model prediction with predictions from existing literature models. Currents have been normalized to the peak current in the initial deactivation step in the sine wave protocol (around 1.6 seconds) as we do not expect the channel to be fully open at the longest T_{step} in these activation kinetics protocols.

F Comparing Cell-Specific with Average Model

In addition to creating cell specific models as described so far we also created an averaged model by first normalizing each experimental trace to one reference trace (so that each trace was given equal weight in the averaging regardless of the conductance of the channel) and then summing and averaging the current value at each time point along the protocol.

The parameter values obtained when calibrating each cell-specific and averaged model are shown in Table F11. These values correspond to the parameter sets with maximum posterior density identified in the MCMC chain. The full posterior density distributions for each parameter for each of the 9 cells are shown in Figure F7.

Table F11: Table of parameter values at the maximum posterior density for each cell-specific model, and the model fitted to averaged data. Here the model parameter numberings correspond to those detailed in Figure 3B, and G_{Kr} represents the conductance value fitted for each model. *Note that the conductance fitted for the ‘Averaged’ model reflects mainly the conductance for the reference experimental trace (used for scaling all other traces before averaging), and should not be considered the ‘average’ conductance, hence its omission from Figure 6A.

	P_1	P_2	P_3	P_4	P_5	P_6	P_7	P_8	G_{Kr}
Cell #1	1.9742×10^{-4}	0.0594	7.1664×10^{-5}	0.0493	0.1048	0.0139	0.0038	0.0360	0.1350
Cell #2	3.2387×10^{-4}	0.0653	7.8183×10^{-5}	0.0497	0.0805	0.0025	0.0049	0.0324	0.0902
Cell #3	4.7883×10^{-4}	0.0661	5.1621×10^{-5}	0.0523	0.1375	0.0094	0.0039	0.0375	0.1011
Cell #4	6.7417×10^{-4}	0.0563	5.8605×10^{-5}	0.0516	0.0893	0.0057	0.0059	0.0324	0.0743
Cell #5	2.2578×10^{-4}	0.0699	3.4477×10^{-5}	0.0546	0.0873	0.0089	0.0052	0.0316	0.1524
Cell #6	6.1015×10^{-4}	0.0662	1.2729×10^{-4}	0.0380	0.0810	0.0165	0.0092	0.0253	0.0218
Cell #7	5.5188×10^{-4}	0.0477	6.6263×10^{-5}	0.0457	0.0628	0.0087	0.0054	0.0317	0.1555
Cell #8	3.1062×10^{-4}	0.0485	5.0455×10^{-5}	0.0491	0.0722	0.0063	0.0060	0.0328	0.0983
Cell #9	5.5916×10^{-4}	0.0435	1.2377×10^{-4}	0.0444	0.0658	0.0028	0.0036	0.0343	0.0514
Averaged	4.0177×10^{-4}	0.0578	6.5137×10^{-5}	0.0487	0.0807	0.0068	0.0052	0.0334	0.0673*

To quantitatively compare the average model predictions and the cell-specific model predictions shown in Figure 6B of the main text we calculated the mean square difference at each point between the average model and the cell-specific models for each cell when predicting the full current trace in response to the steady-state activation protocol. We also repeated this for the deactivation and inactivation protocols and the action potential protocol shown in Figures 4 and 5. The differences for each cell are shown in Table F12 with a comparison between the experimental result and the average model predictions with the cell-specific predictions.

We note that we have ordered the cells in this table (as in Figure 6) according to the percentage change in leak resistance between performing the vehicle and dofetilide repeats of the sine wave voltage protocol used to construct the model. This ordering acts as an estimated ranking for the quality of each recording. The benefit of a cell-specific approach occurs when using the highest quality data for both model construction and validation. We should note that even though in cells #4 and #6 the average model provides the better prediction of the steady-state activation peak current-voltage relationship than the cell-specific model, the cell-specific models are still providing very good predictions in these cases, it is just that the experimental behavior is more like the average model behavior for these cells. We also note that for six out of the nine cells, the cell-specific model provides a better prediction of the current response to the action potential protocol than the average model, however, in the cases where the cell-specific model is worse the difference is only a small amount.

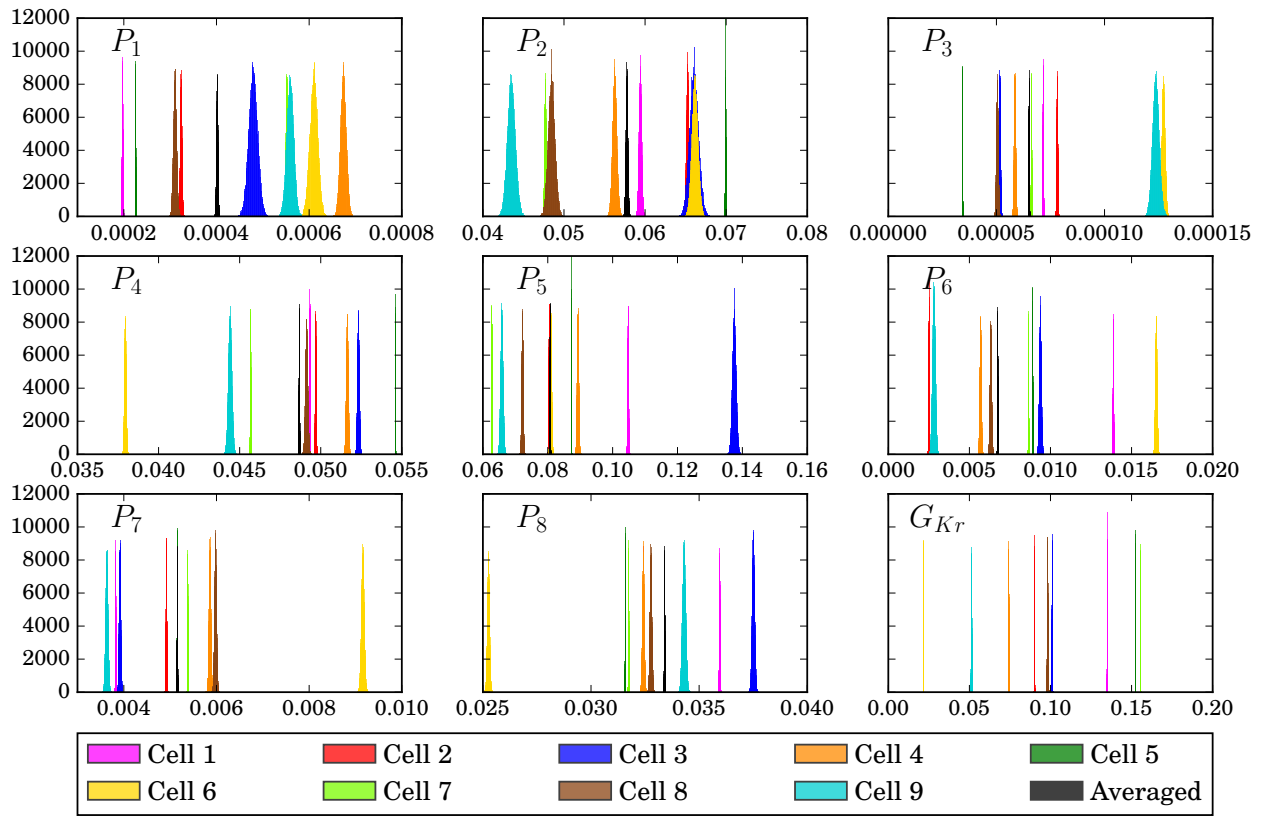


Figure F7: Distributions for each parameter for each of the 9 cell-specific models and the averaged data model. To aid comparison these are all histograms with 100 bars (plotting probability distributions here leads to very different maxima, obscuring the spread information), and so the y-axis is in arbitrary units related to the number of samples. We see that the parameter values tend to be given distinct distributions and so we would consider most of them to be ‘significantly different’.

We use a measure of

$$\text{error} = \left(\frac{1}{T} \sum_{t=1}^T (\text{simulated current at time step } t - \text{experimental current at time step } t)^2 \right)^{\frac{1}{2}}, \quad (\text{F.3})$$

828 to evaluate the error in model predictions for individual cells (using the whole current traces, apart
829 from removing regions in the sine wave protocol with capacitive spikes as explained in Online
830 Methods 4.7.1).

Table F12: Table showing the error measure defined by equation F.3 between cell-specific or average models and the experimental current recording for fit (sine wave Pr7) and predictions with validation protocols (all other columns). Cells are ordered in ascending order according to the percentage change in leak resistance R_{leak} . Here the color scale is set so that within each pair of columns represents lowest error and represents the highest error for each protocol/pair of columns. Note that the cells with larger currents will show larger errors, but the left column cell-specific predictions tend to perform better than the average model, particularly for cells where the average model gives a relatively large error.

Cell #	ΔR_{leak} (%)	Sine Wave (Pr 7)		APs (Pr 6)		Steady Act. (Pr 3)		Deact. (Pr 4)		Inact. (Pr 5)	
		Specific	Average	Spec.	Aver.	Spec.	Aver.	Spec.	Aver.	Spec.	Aver.
1	0.0	0.0268	0.0650	0.0757	0.1195	0.0745	0.1369	0.2115	0.2334	0.1312	0.1250
2	7.7	0.0262	0.0401	0.0549	0.0516	0.0481	0.0490	0.1421	0.1249	0.0478	0.0489
3	12.5	0.0348	0.0609	0.0997	0.1403	0.0917	0.1489	0.1320	0.1317	0.1106	0.1600
4	16.7	0.0346	0.0497	0.0649	0.0690	0.0931	0.0797	0.1337	0.1301	0.0864	0.0959
5	20.0	0.0338	0.0374	0.1003	0.1149	0.0964	0.1274	0.2788	0.3358	0.5713	0.5668
6	28.6	0.0149	0.0335	0.0419	0.0401	0.0482	0.0372	0.0883	0.0739	0.0443	0.0419
7	32.5	0.0825	0.1073	0.1343	0.1635	0.2060	0.1772	0.3167	0.3595	0.1239	0.1398
8	42.9	0.0426	0.0514	0.1331	0.1356	0.1302	0.1494	0.1796	0.2345	0.2222	0.2233
9	58.3	0.0243	0.0266	0.1478	0.1472	0.1109	0.1068	0.1806	0.1766	0.2183	0.2174

831 For predictions of the action potential protocol currents, Table F12 demonstrates that the cell-
832 specific modeling approach yields predictions that are very close to or better than the average model.
833 Additionally, for the predictions of the steady-state activation protocol the cell-specific approach
834 generally yields very good and more accurate (for 4/5) predictions of validation data when the
835 highest quality data is used (cells #1–5). This benefit is absent when lower quality experimental
836 data is used where the average model provides very similar, but slightly better, predictions (cells
837 #6–9).

838 We also compare cell-specific and average predictions for each of the 9 cells for the deactivation,
839 recovery from inactivation and instantaneous inactivation time constants as were shown for one
840 cell in Figure 4. We show this comparison for each cell in Figure F8 and F9 for 8/9 cells and in
841 Figure F10 for all cells. Cell #6 was omitted in the first two plots because this cell had a particularly
842 low current and it was difficult to accurately fit exponential curves to the experimental data for
843 this cell. We also note that we have not plotted the time constant values for -90 mV in Figures F8
844 & F9 for the same reason; we could not confidently fit an exponential decay curve to determine an
845 accurate time constant value for this voltage step.

846 We see in Figures F8–F10 that the same observations that were made for the results shown in
847 Figure 6 generally hold: for lower cell numbers #1–5, we see enhanced predictions of the experi-
848 mental time constants from the cell-specific model rather than the averaged model. i.e predictions

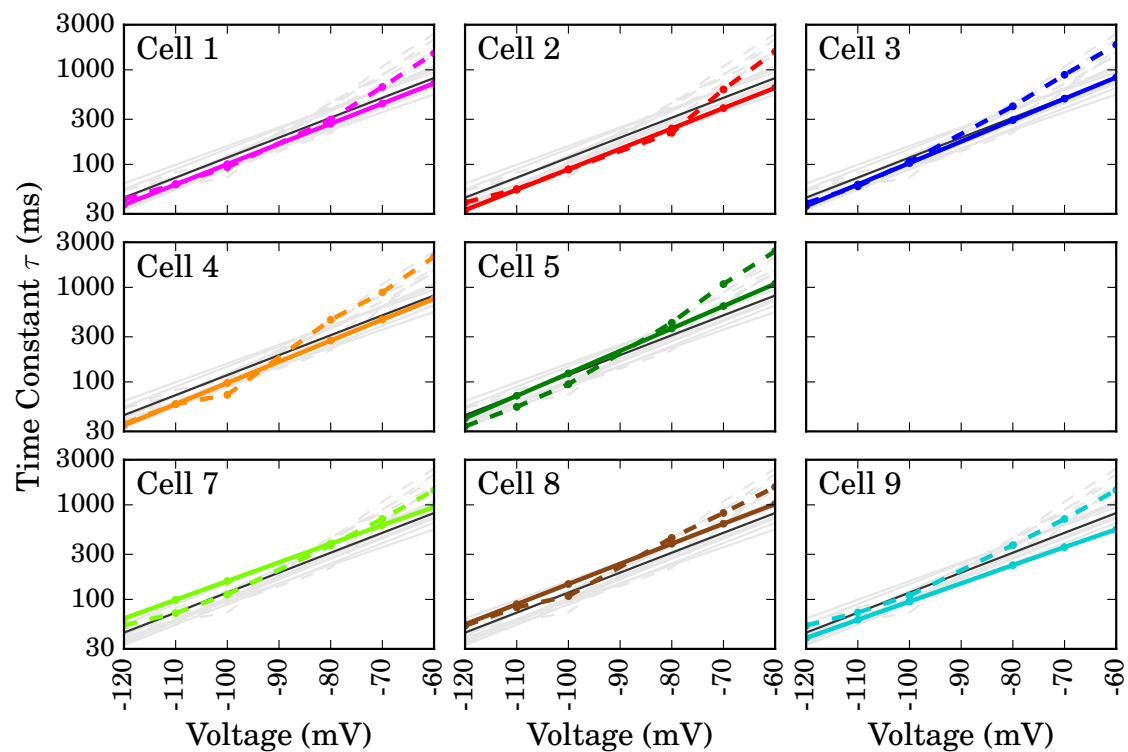


Figure F8: Cell-specific model predictions of time constant/voltage relationships for deactivation (Pr5). Each plot represents a different cell, with cell-specific model prediction depicted by the bold line, and the dashed line showing the cell's experimental data. Black lines on each plot represents the average model prediction. Cells are ordered as in Table F12.

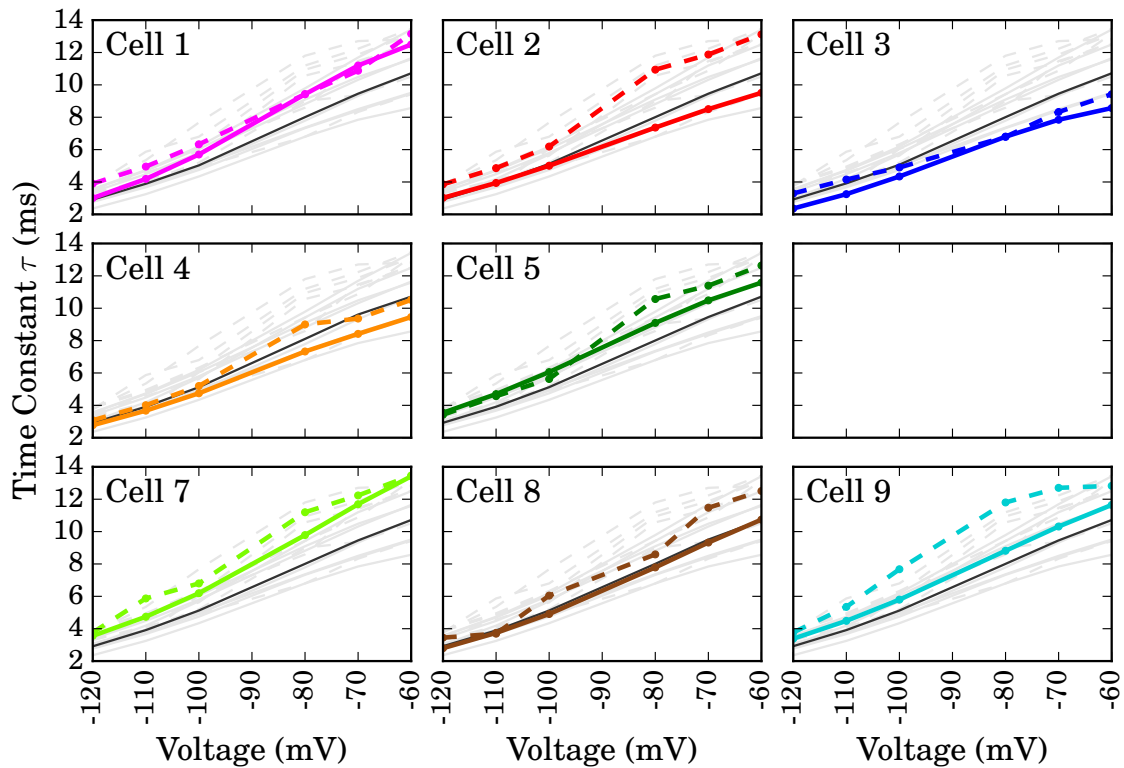


Figure F9: Cell-specific model predictions of time constant/voltage relationships for recovery from inactivation in Pr5. Each plot represents a different cell, with cell-specific model prediction depicted by the bold line, and the dashed line showing the cell's experimental data. Black lines on each plot represents the average model prediction. Cells are ordered as in Table F12.

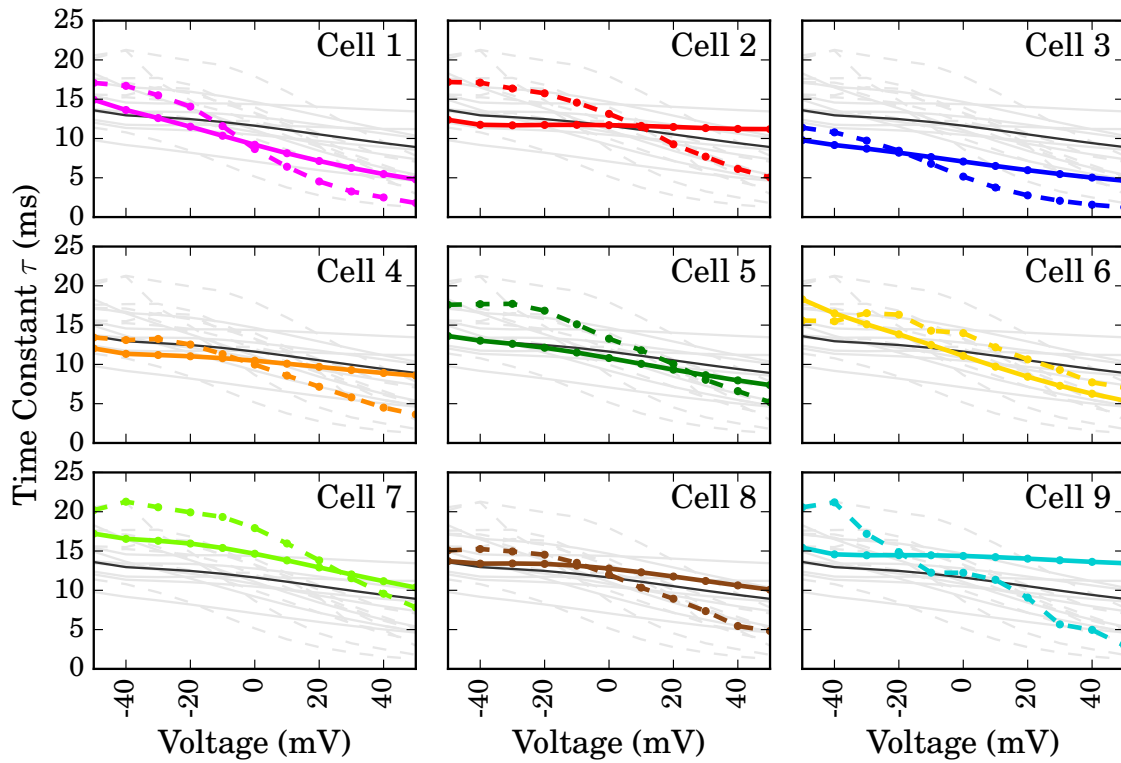


Figure F10: Cell-specific model predictions of time constant/voltage relationships for instantaneous inactivation (Pr4). Each plot represents a different cell, with cell-specific model prediction depicted by the bold line, and the dashed line showing the cell's experimental data. Black lines on each plot represents the average model prediction. Cells are ordered as in Table F12.

849 are better in the cells with lower percentage changes in leak current resistance, which correspond
850 to better quality data.

851 References

- 852 2. Vandenberg, J. *et al.* hERG K⁺ channels: Structure, function, and clinical significance. *Phys-*
853 *iological Reviews* **92**, 1393–1478 (2012).
- 854 25. Wang, S., Liu, S., Morales, M., Strauss, H. & Rasmusson, R. A quantitative analysis of the
855 activation and inactivation kinetics of HERG expressed in *Xenopus* oocytes. *The Journal of*
856 *Physiology* **502**, 45–60 (1997).
- 857 30. Zeng, J., Laurita, K. R., Rosenbaum, D. S. & Rudy, Y. Two components of the delayed rectifier
858 K⁺ current in ventricular myocytes of the guinea pig type theoretical formulation and their
859 role in repolarization. *Circulation Research* **77**, 140–152 (1995).
- 860 31. Mazhari, R., Greenstein, J., Winslow, R., Marbán, E. & Nuss, H. Molecular interactions be-
861 tween two Long-QT syndrome gene products, HERG and KCNE2, rationalized by in vitro and
862 in silico analysis. *Circulation Research* **89**, 33–38 (2001).
- 863 32. Ten Tusscher, K., Noble, D., Noble, P. & Panfilov, A. A model for human ventricular tissue.
864 *American Journal of Physiology-Heart and Circulatory Physiology* **286**, H1573–H1589 (2004).
- 865 33. Di Veroli, G., Davies, M., Zhang, H., Abi-Gerges, N. & Boyett, M. High-throughput screening
866 of drug-binding dynamics to HERG improves early drug safety assessment. *American Journal*
867 *of Physiology-Heart and Circulatory Physiology* **304**, H104–H117 (2013).
- 868 42. Walch, O. J. & Eisenberg, M. C. Parameter identifiability and identifiable combinations in
869 generalized Hodgkin–Huxley models. *Neurocomputing* **199**, 137–143 (2016).
- 870 43. Haario, H., Saksman, E. & Tamminen, J. An Adaptive Metropolis Algorithm. *Bernoulli*, 223–
871 242 (2001).
- 872 44. Gilks, W. R., Richardson, S. & Spiegelhalter, D. J. *Markov chain Monte Carlo in practice*
873 (London: Chapman and Hall, 1996).
- 874 45. Kiehn, J., Lacerda, A. & Brown, A. Pathways of HERG inactivation. *American Journal of*
875 *Physiology-Heart and Circulatory Physiology* **277**, H199–H210 (1999).
- 876 46. Piper, D., Varghese, A., Sanguinetti, M. & Tristani-Firouzi, M. Gating currents associated
877 with intramembrane charge displacement in HERG potassium channels. *Proceedings of the*
878 *National Academy of Sciences* **100**, 10534 (2003).
- 879 47. Lindblad, D., Murphey, C., Clark, J. & Giles, W. A model of the action potential and under-
880 lying membrane currents in a rabbit atrial cell. *American Journal of Physiology* **271**, H1666–
881 H1696 (1996).
- 882 48. Liu, S., Rasmusson, R., Campbell, D., Wang, S. & Strauss, H. Activation and inactivation
883 kinetics of an E-4031-sensitive current from single ferret atrial myocytes. *Biophysical Journal*
884 **70**, 2704–2715 (1996).
- 885 49. Courtemanche, M., Ramirez, R. & Nattel, S. Ionic mechanisms underlying human atrial action
886 potential properties: Insights from a mathematical model. *American Journal of Physiology-*
887 *Heart and Circulatory Physiology* **275**, H301–H321 (1998).
- 888 50. Nygren, A. *et al.* Mathematical model of an adult human atrial cell the role of K⁺ currents in
889 repolarization. *Circulation Research* **82**, 63–81 (1998).

- 890 51. Priebe, L. & Beuckelmann, D. J. Simulation study of cellular electric properties in heart failure.
891 *Circulation Research* **82**, 1206–1223 (1998).
- 892 52. Winslow, R. L., Rice, J., Jafri, S., Marban, E. & O'Rourke, B. Mechanisms of altered excitation-
893 contraction coupling in canine tachycardia-induced heart failure, II Model studies. *Circulation*
894 *Research* **84**, 571–586 (1999).
- 895 53. Ramirez, R. J., Nattel, S. & Courtemanche, M. Mathematical analysis of canine atrial action
896 potentials: rate, regional factors, and electrical remodeling. *American Journal of Physiology-
897 Heart and Circulatory Physiology* **279**, H1767–H1785 (2000).
- 898 54. Zhang, H. *et al.* Mathematical models of action potentials in the periphery and center of the
899 rabbit sinoatrial node. *American Journal of Physiology-Heart and Circulatory Physiology* **279**,
900 H397–H421 (2000).
- 901 55. Clancy, C. & Rudy, Y. Cellular consequences of HERG mutations in the long QT syndrome:
902 Precursors to sudden cardiac death. *Cardiovascular Research* **50**, 301–313 (2001).
- 903 56. Lu, Y. *et al.* Effects of premature stimulation on HERG K⁺ channels. *The Journal of Physi-
904 ology* **537**, 843–851 (2001).
- 905 57. Fox, J. J., McHarg, J. L. & Gilmour Jr, R. F. Ionic mechanism of electrical alternans. *American
906 Journal of Physiology-Heart and Circulatory Physiology* **282**, H516–H530 (2002).
- 907 58. Kurata, Y., Hisatome, I., Imanishi, S. & Shibamoto, T. Dynamical description of sinoatrial
908 node pacemaking: improved mathematical model for primary pacemaker cell. *American Jour-
909 nal of Physiology-Heart and Circulatory Physiology* **283**, H2074–H2101 (2002).
- 910 59. Oehmen, C., Giles, W. & Demir, S. Mathematical model of the rapidly activating delayed
911 rectifier potassium current IKr in rabbit sinoatrial node. *Journal of Cardiovascular Electro-
912 physiology* **13**, 1131–1140 (2002).
- 913 60. Matsuoka, S., Sarai, N., Kuratomi, S., Ono, K. & Noma, A. Role of individual ionic current
914 systems in ventricular cells hypothesized by a model study. *The Japanese Journal of Physiology*
915 **53**, 105–123 (2003).
- 916 61. Seemann, G., Sachse, F. B., WEIB, D. L. & DÖSSEL, O. Quantitative reconstruction of car-
917 diac electromechanics in human myocardium. *Journal of Cardiovascular Electrophysiology* **14**,
918 S219–S228 (2003).
- 919 62. Hund, T. J. & Rudy, Y. Rate dependence and regulation of action potential and calcium
920 transient in a canine cardiac ventricular cell model. *Circulation* **110**, 3168–3174 (2004).
- 921 63. Shannon, T., Wang, F., Puglisi, J., Weber, C. & Bers, D. A mathematical treatment of in-
922 tegrated Ca dynamics within the ventricular myocyte. *Biophysical Journal* **87**, 3351–3371
923 (2004).
- 924 64. Fink, M., Noble, D., Virag, L., Varro, A. & Giles, W. R. Contributions of HERG K⁺ current to
925 repolarization of the human ventricular action potential. *Progress in Biophysics and Molecular
926 Biology* **96**, 357–376 (2008).
- 927 65. Aslanidi, O. V., Stewart, P., Boyett, M. R. & Zhang, H. Optimal velocity and safety of dis-
928 continuous conduction through the heterogeneous Purkinje-ventricular junction. *Biophysical
929 Journal* **97**, 20–39 (2009).
- 930 66. Inada, S., Hancox, J., Zhang, H. & Boyett, M. One-dimensional mathematical model of the
931 atrioventricular node including atrio-nodal, nodal, and nodal-his cells. *Biophysical Journal* **97**,
932 2117–2127 (2009).

- 933 67. Grandi, E., Pasqualini, F. S. & Bers, D. M. A novel computational model of the human
934 ventricular action potential and Ca transient. *Journal of Molecular and Cellular Cardiology*
935 **48**, 112–121 (2010).
- 936 68. O’Hara, T., Virág, L., Varró, A. & Rudy, Y. Simulation of the undiseased human cardiac ven-
937 tricular action potential: model formulation and experimental validation. *PLoS Computational*
938 *Biology* **7**, e1002061 (2011).
- 939 69. Severi, S., Fantini, M., Charawi, L. A. & DiFrancesco, D. An updated computational model
940 of rabbit sinoatrial action potential to investigate the mechanisms of heart rate modulation.
941 *The Journal of Physiology* **590**, 4483–4499 (2012).